A Two-Step Motion Compensation Method for Polar Format Images of Terahertz SAR Based on Echo Data

Shaowen Luo, Qiuyan Wang, Yinwei Li, *Member, IEEE*, Xiaolong Chen, and Yiming Zhu, *Senior Member, IEEE*

***Abstract*—Terahertz synthetic aperture radar (THz SAR) has great potential in the field of remote sensing due to its high resolution and high frame rate. However, THz SAR is very sensitive to motion errors, making even small 2-D error caused by motion error and polar format algorithm (PFA) seriously affect the image quality. Existing microwave SAR autofocusing methods only estimate the error of a single dimension, which cannot meet the accuracy requirements of THz SAR for 2-D error compensation. In this article, a two-step motion compensation method for polar format images of THz SAR based on echo data is proposed. First, by analyzing the conversion model of polar coordinate format, the node where the 2-D error coupling occurs is determined. On this basis, a coarse compensation based on low-frequency fitting is proposed in front of this node to reduce the influence of PFA on the error coupling of 2-D signals. The method not only preserves the correction of the inherent range cell migration by PFA but also eliminates the interference of PFA to the subsequent error compensation processing. Second, to solve the problem that a single compensation method cannot meet the accuracy requirements of THz SAR, the maximum contrast method after polar coordinate format conversion is used for precision compensation. The effectiveness of the proposed method is verified through simulation and actual measurement data processing of 0.22-THz airborne spotlight SAR system.**

***Index Terms*—Low-frequency fitting, maximum contrast, polar format algorithm (PFA), range cell migration (RCM), terahertz synthetic aperture radar (THz SAR).**

I. Introduction

SYNTHETIC aperture radar (SAR) is a sophisticated remote sensing technology [1], [2], [3] that synthesizes large apertures by collecting data from mobile radar antennas. SAR is capable of producing high-resolution images regardless of adverse weather conditions or the absence of light, making it a crucial tool in environmental monitoring, military reconnaissance, Earth observation, and various other remote sensing applications [4], [5]. With the advancement of SAR technology, terahertz SAR (THz SAR), as a new branch of SAR technology, has been widely concerned [6], [7], [8]. THz SAR offers remarkable improvements over the traditional SAR, including higher resolution and higher frame rates. These enhancements make THz SAR highly promising in advanced remote sensing applications, such as ground-moving target detection and tracking, and security inspections [9], [10].

However, the higher resolution images of THz SAR systems also bring new challenges, especially in terms of motion error compensation [11], [12]. In practical applications, the nonideal motion of the moving platform leads to motion errors, resulting in the phase errors and range cell migration (RCM) errors in echo signal [13]. If these errors are not compensated, the resulting echo signals will lead to ghosting, defocusing, and distortion of imaging results, thus reducing the image quality and even making the image unrecognizable [14]. Compared with microwave SAR, THz SAR is very sensitive to motion errors. Even small platform motion error can result in a significant reduction in image quality. This puts forward higher requirements for motion error compensation.

The motion error compensation methods in SAR imaging can be divided into two categories: the error compensation method based on difference global positioning system and inertial measurement unit (DGPS/IMU) [15], [16] and the autofocus method based on echo data [17], [18]. In general, the compensation accuracy based on DGPS and IMU cannot meet the imaging requirements of high-resolution SAR. Even after compensation based on DGPS and IMU, there are still some residual errors, which need to be compensated by autofocus algorithms [19], [20]. Autofocus algorithms in microwave SAR are mainly used to compensate 1-D azimuth phase error (APE), which ignores the influence of residual RCM. When the residual RCM is larger than the range resolution, the compensation strategy will fail [21], [22]. However, in THz high-resolution SAR imaging, the residual RCM often cannot be ignored, and such a strategy that only compensates APE will reduce the accuracy of nonparametric autofocus methods [23]. Therefore, it is crucial to compensate both APE and residual RCM in THz SAR imaging.

Received 4 July 2024; revised 16 August 2024; accepted 3 September 2024. Date of publication 13 September 2024; date of current version 30 September 2024. This work was supported in part by the National Natural Science Foundation of China under Grant 61988102 and Grant 12105177, in part by the Natural Science Foundation of Shanghai under Grant 21ZR1444300, and in part by Basic Strengthening Program Technical Area Fund under Grant 2023-JCJQ-JJ-0108. *(Corresponding author: Yinwei Li.)*

Shaowen Luo, Qiuyan Wang, and Xiaolong Chen are with the School of Optical-Electrical and Computer Engineering, University of Shanghai for Science and Technology, Shanghai 200093, China (e-mail: 213330652@st.usst.edu.cn; 223330692@st.usst.edu.cn; 232200391@st.usst.edu.cn).

Yinwei Li is with the Terahertz Technology Innovation Research Institute, Terahertz Spectrum and Imaging Technology Cooperative Innovation Center, University of Shanghai for Science and Technology, Shanghai 200093, China, also with the School of Intelligent Emergency Management, University of Shanghai for Science and Technology, Shanghai 200093, China, and also with the Shanghai Institute of Intelligent Science and Technology, Tongji University, Shanghai 200092, China (e-mail: liyw@usst.edu.cn).

Yiming Zhu is with the Terahertz Technology Innovation Research Institute, Terahertz Spectrum and Imaging Technology Cooperative Innovation Center, University of Shanghai for Science and Technology, Shanghai 200093, China (e-mail: ymzhu@usst.edu.cn).

Digital Object Identifier 10.1109/JSTARS.2024.3461332

To date, most 2-D motion error compensation studies have been based on microwave SAR. However, microwave SAR has longer wavelengths and lower resolution than THz SAR, making it more tolerant of 2-D motion errors. Therefore, the 2-D motion error compensation methods developed for microwave SAR systems often have some shortcomings and inadequacies when they are directly applied to THz SAR, such as reduced resolution or neglecting the influence of 2-D error coupling [24], [25].

Current research on the motion error compensation of THz SAR primarily focuses on the high-frequency vibration errors [26], [27], [28]. Due to the lack of THz SAR measurement data, most of these studies are simulation-based research conducted using laboratory data and have limited practical applications. The actual motion errors in airborne THz SAR are very complex, encompassing not only high-frequency vibration errors but also low-frequency motion errors [29], [30].

Some errors not considered in microwave SAR compensation methods will also affect the image quality of THz SAR, such as 2-D coupling errors caused by imaging algorithms. A novel 2-D autofocusing algorithm is proposed for addressing the issue of 2-D defocusing in airborne strip map THz SAR imaging [31]. However, this method mainly compensates for range amplitude and phase errors caused by nonideal THz devices, and does not solve the 2-D coupling errors caused by the imaging algorithm itself.

Polar format algorithm (PFA) realizes 2-D decoupling of SAR images through 2-D resampling in the wavenumber domain [32], [33]. This resampling results in a 2-D coupling of APE and residual RCM [34]. Considering the error sensitivity of THz SAR, this type of coupling leads to severe defocusing of 2-D images. Additionally, due to the high resolution of THz SAR, such 2-D defocusing greatly interferes with the selection of the main scatterers, reducing the accuracy of autofocus algorithms that depend on the scatterer's selection. Therefore, 2-D error compensation of THz SAR requires more detailed and specific attention.

To solve the above problems, this article proposes a two-step motion compensation method for polar format images of THz SAR based on echo data. The main contributions of this article to THz spotlight SAR autofocus are as follows.

1) The causes of motion error coupling in the PFA algorithm are analyzed theoretically, and the node where the motion error coupling occurs is determined, which provides a theoretical basis for the subsequent improvement of the motion error compensation method.
2) A two-step motion compensation approach, consisting of coarse compensation and fine compensation, is proposed for terahertz PFA images based on echo data. The proposed coarse-compensation method based on low-frequency fitting is adjusted to be performed before the keystone transformation step, which minimizes the 2-D coupling of motion errors caused by PFA while retaining its ability to eliminate inherent RCM. Then, after coarse compensation and intrinsic RCM correction (RCMC), the maximum contrast algorithm (MCA) is used for fine compensation to meet the high compensation accuracy requirements of THz SAR, so as to obtain high quality images.
3) The effectiveness of the proposed method is verified through simulation and actual measurement data processing of 0.22-THz airborne spotlight SAR system.

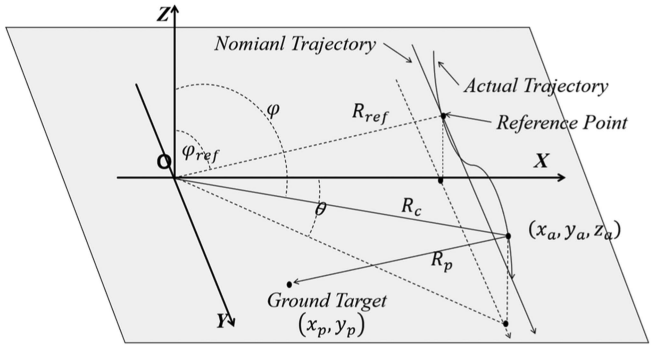

Fig. 1. Geometric model of spotlight SAR echo acquisition.

The rest of this article is organized as follows. Section II establishes the model of 2-D errors for PFA. Based on the established model, Section III proposes an estimation and compensation method to eliminate the effects of 2-D errors on the imaging results of THz SAR. Section IV validates the effectiveness of the proposed method through simulation experiments and actual measurement results. Section V presents the discussion. Finally, Section VI concludes this article.

II. Signal Model

A. Polar Format Algorithm

The geometric model of THz spotlight SAR for collecting echo signal data is illustrated in Fig. 1. To mimic the real-world application scenarios, the radar platform is assumed to move along a nonuniform trajectory that deviates from an ideal straight line. The *XYZ* coordinate system is established with scene center *O* as the origin and the *X*-axis, *Y*-axis, and *Z*-axis represent the range, azimuth, and height directions, respectively. The instantaneous position of the phase center of the radar antenna in this coordinate system is denoted as (x_a, y_a, z_a), and the corresponding instantaneous pitch angle and azimuth angle are denoted as φ and θ, respectively. When taking the moment of the synthetic aperture center as the origin of azimuth slow time, the corresponding instantaneous pitch angle can be regarded as the reference pitch angle, denoted as φ_{ref}. For a point target (x_p, y_p) in the scene, the instantaneous range from the phase center of the radar antenna to the point is denoted as R_p, R_c represents the instantaneous slant range between the radar platform and the scene center, and R_{ref} is the reference slant range between the reference point of radar platform and the scene center.

When the radar emits a wideband signal to the detection scene, the signal can be represented as follows:

$$S_t(\tau) = A \cdot \exp\left(j2\pi f_c \tau + j\pi K_r \tau^2\right) \tag{1}$$

where f_c is the center frequency of transmitted linear frequency-modulated signal, K_r is the frequency modulation rate, τ represents the fast time, and A denotes the amplitude value of the transmitted signal.

The signal that returns after interacting with the target and undergoes dechirping can be represented as follows:

$$S_d(t, f_r) = A \cdot \exp\left[j\frac{4\pi}{c}(f_c + f_r)\Delta R(t)\right] \tag{2}$$

where t is the azimuth slow time, f_r is the signal frequency in the range direction, ΔR is the difference range between the radar to the corresponding target point and the scene center target point, and $\Delta R(t) = R_c - R_p = R_b(t) + R_e(t)$. $R_b(t)$ is the baseline term in the difference range. And $R_e(t)$ is the range error term and can be expressed as

$$\begin{aligned} R_e(t) &= \Delta R(t) - R_b(t) \\ &= \sqrt{(R_{\text{ref}}\sin\varphi_{\text{ref}} + x_p)^2 + (V_a t + y_p)^2 + H^2} \\ &\quad - \sqrt{\begin{matrix}(R_{\text{ref}}\sin\varphi_{\text{ref}} + x_p + E_x(t))^2 \\ +(V_a t + y_p + E_y(t))^2 \\ +(H + E_z(t))^2\end{matrix}} \end{aligned} \tag{3}$$

where $E_x(t)$, $E_y(t)$, and $E_z(t)$ represent the offsets of radar antenna along the *X*-axis, *Y*-axis, and *Z*-axis, respectively. *H* denotes the height of the platform, and V_a represents the ideal velocity of the platform in the azimuth direction.

Based on the plane wave assumption, $R_b(t)$ in (2) can be simplified as follows:

$$R_b(t) = \sin\varphi(x_p\sin\theta + y_p\cos\theta). \tag{4}$$

Subsequently, the signal in (2) can be represented as follows:

$$\begin{aligned} S_d(t, f_r) = A \cdot \exp\Bigg\{ & j\frac{4\pi}{c}(f_c + f_r) \\ & \times [\sin\varphi(x_p\sin\theta + y_p\cos\theta) + R_e(t)]\Bigg\}. \end{aligned} \tag{5}$$

According to Mao and Zhu [34], PFA 2-D format resampling can be interpreted as frequency modulation of range dimension, RCM linearization, and Keystone transformation. In (5), the frequency modulation of range dimension is defined as

$$f_r = \delta_r f_r + f_c(\delta_r - 1) \tag{6}$$

where $\delta_r = \sin\varphi_{\text{ref}}/(\sin\varphi\cos\theta)$ is the frequency modulation factor in range dimension, and $f_c(\delta_r - 1)$ is the corresponding offset of the signal $S_d(t, f_r)$. Therefore, after range resampling, the signal in range dimension can be expressed as follows:

$$\begin{aligned} S_{R1}(t, f_r) = A \cdot \exp\Bigg\{ & j\frac{4\pi}{c}(f_c + f_r) \\ & \times \sin\varphi_{\text{ref}}[(x_p\tan\theta + y_p) + \epsilon(t)]\Bigg\} \end{aligned} \tag{7}$$

where $\epsilon(t) = R_e(t)/(\sin\varphi\cos\theta)$.

Then, the format transformation of the signal in the azimuth dimension is divided into two steps: RCM linearization and Keystone transformation. RCM linearization does not involve any change in range frequency. It is just a pure transformation of the azimuth angle with time, that is, $t = \vartheta_a(t)$.

The signal simplified expression after RCM linearization is

$$\begin{aligned} S_{A1}(t, f_r) = A \cdot \exp\{ & j\,4\pi(f_c + f_r)\sin\varphi_{\text{ref}}/C \\ & \times [x_p\Omega t + y_p + \eta(t)]\} \end{aligned} \tag{8}$$

where $\Omega = V_a/R_c$ represents the angular velocity of the radar platform motion, and $\eta(t) = \epsilon[\vartheta_a(t)]$.

Let $t = \frac{f_c}{f_c + f_r}t$, complete the Keystone transformation of (8), and obtain the decoupled 2-D signal, which is denoted as follows:

$$\begin{aligned} S_{A2}(t, f_r) = A \cdot \exp\Bigg\{ & j\frac{4\pi\sin\varphi_{\text{ref}}}{c}[f_c x_p\Omega t \\ & + (f_c + f_r)y_p] + \Phi\Bigg\} \end{aligned} \tag{9}$$

where $\Phi = \frac{4\pi\sin\varphi_{\text{ref}}}{c}(f_c + f_r)\eta(\frac{f_c}{f_c + f_r}t)$ is the remaining 2-D phase error in the spatial frequency domain.

The above is the complete process of PFA. To facilitate the observation variable relationships, through introducing $X = \frac{4\pi\sin\varphi_{\text{ref}}}{c}f_c\Omega t$ and $Y = \frac{4\pi\sin\varphi_{\text{ref}}}{c}(f_c + f_r)$, (9) can be simplified as follows:

$$S_{A2}(X, Y) = A \cdot \exp\left\{j\left[Xx_p + Yy_p + Y\chi\left(\frac{X}{Y}\right)\right]\right\} \tag{10}$$

where $\chi(X) = \eta(\frac{X}{\Omega})$ and $\Phi = Y\chi(\frac{X}{Y})$.

By performing a 2-D fast Fourier transform (FFT) on (10), the compressed 2-D image can be obtained. However, the 1-D motion error in the echo signal is not compensated, and the 2-D coupling of the error occurs during the polar coordinate transformation, resulting in serious 2-D defocusing and distortion of the image. Because the traditional motion error compensation methods are usually processed after the 2-D error coupling, it will make the traditional error compensation methods ineffective.

B. 2-D Error Modeling

As can be seen from (8), the error term $\eta(t)$ still appears in 1-D form. However, after the Keystone transformation, $\eta(t)$ is transformed into $\eta(f_c t/(f_c + f_r))$, where the error term becomes the Φ state of range–azimuth 2-D coupling. In order to facilitate the analysis of the change of motion error, we decompose the 2-D phase error in (9) as follows:

$$\begin{aligned} \Phi(X) &= \phi_0(X) + \phi_1(X) \cdot f_r \\ \phi_0(X) &= \frac{4\pi\sin\varphi_{\text{ref}}}{c}f_c\eta\left(\frac{f_c}{f_c + f_r}t\right) \\ \phi_1(X) &= \frac{4\pi\sin\varphi_{\text{ref}}}{c}\eta\left(\frac{f_c}{f_c + f_r}t\right) \end{aligned} \tag{11}$$

where $\phi_0(X)$ represents the APE after 2-D coupling, and $\phi_1(X)$ denotes the residual RCM after 2-D coupling.

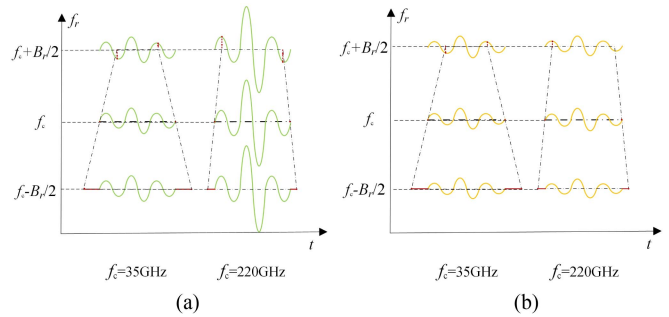

Fig. 2. Illustration of 2-D error visualization for different carrier frequencies. (a) APE. (b) Residual RCM.

It can be seen from (11) that the azimuth error and range error change dramatically with the increase of the carrier frequency of SAR system. For SAR systems of different bands, Fig. 2 gives the variation of azimuth error and range error in 2-D space after processing by PFA. In Fig. 2(a), the left side shows the APE for 35-GHz SAR system, while the right side shows the APE for 220-GHz SAR system. In Fig. 2(b), the left side shows the residual RCM for 35-GHz SAR system, while the right side shows the residual RCM for 220-GHz SAR system. When the platform motion errors are the same, the magnitude of APE increases proportionally with the increase of the carrier frequency f_c, but the residual RCM does not change. Moreover, both errors are scaled to a certain extent in range direction. As shown by $\chi(\frac{X}{Y})$, this phenomenon becomes less pronounced when the difference between carrier frequency and range frequency is large.

Hence, it is evident that PFA introduces additional spatially varying errors at a certain ratio. Although the spatial change rate decreases with the increase of carrier frequency, it is well known that the higher the carrier frequency, the larger the amplitude of APE, where the amplitude change ratio of APE is $S_{\text{amp}} = f_{c1}/f_{c2}$.

In addition, PFA also has the effect of scale transformation on the error. According to the Keystone transformation of $t = \frac{f_c}{f_c+f_r}t$ performed by (9), the maximum azimuth scale difference between the nearest and furthest slant range for different carrier frequency systems after PFA treatment is shown as follows:

$$\begin{aligned} Lin1_{\max} &= \frac{f_{c1}}{f_{c1}-B_r/2} - \frac{f_{c1}}{f_{c1}+B_r/2} \\ &= \frac{f_{c1}B_r}{{f_{c1}}^2 - {B_r}^2/4} \end{aligned} \tag{12}$$

$$\begin{aligned} Lin2_{\max} &= \frac{f_{c2}}{f_{c2}-B_r/2} - \frac{f_{c2}}{f_{c2}+B_r/2} \\ &= \frac{f_{c2}B_r}{{f_{c2}}^2 - {B_r}^2/4}. \end{aligned} \tag{13}$$

Therefore, the scale scaling ratio S_{cal} between two carrier frequency systems is

$$\begin{aligned} S_{\text{cal}} &= \frac{Lin1_{\max}}{Lin2_{\max}} \\ &= \frac{f_{c1}}{f_{c2}} \frac{{f_{c2}}^2 - {B_r}^2/4}{{f_{c1}}^2 - {B_r}^2/4}. \end{aligned} \tag{14}$$

Observe that the product of S_{amp} and S_{cal} is close to 1. This indicates that there is no change in the linear error under the influence of these two effects, and a more specific analysis is as follows.

The $\Phi = Y\chi(\frac{X}{Y})$ shown in (10) is expanded and the following formula is obtained:

$$\Phi(t) = \check{C}(f_c+f_r)\left[m\frac{f_c}{f_c+f_r}t + n\left(\frac{f_c}{f_c+f_r}t\right)^2 + \cdots\right] \tag{15}$$

where $\check{C}$ represents the irrelevant term in the formula. m and n represent the error coefficients, and the first-order term represents the linear phase in the signal. The above formulation can be simplified as follows:

$$\Phi(t) = \check{C}mf_ct + \check{C}n\frac{(f_ct)^2}{f_c+f_r} + \cdots. \tag{16}$$

It can be seen that for 2-D signals with fixed carrier frequency, the first-order coefficient of phase error after PFA processing is constant, and the second-order coefficient and above will change with the change of range frequency f_r, and the amplitude of change is related to the carrier frequency.

This shows that if the errors in the signal are linear, the carrier frequency does not affect the error coupling caused by PFA. However, in the practical applications, the errors are mainly nonlinear, especially in THz SAR system with shorter wavelengths, where the nonlinearity of errors is more obvious. In this case, as the carrier frequency increases, even if the spatial change rate is slightly reduced, the overall spatial change error value will increase.

The traditional autofocus algorithms only consider 1-D error estimation and compensation, that is, they only deal with 1-D APE and ignore the influence of residual RCM. In general, it is harmless to microwave SAR systems. However, it is not suitable for THz SAR systems with higher carrier frequencies. From (10), it can be deduced that the 2-D coupling error caused by PFA in space is given as follows:

$$\begin{aligned} \Delta\Phi(X,Y) &= \frac{4\pi\sin\varphi_{\text{ref}}}{c}\left[(f_c+f_r)\chi\left(\frac{X}{Y}\right) - f_c\chi\left(\frac{X}{Y_0}\right)\right] \\ &\approx \frac{4\pi\sin\varphi_{\text{ref}}}{c}f_c\left[\chi\left(\frac{X}{Y}\right) - \chi\left(\frac{X}{Y_0}\right)\right] \end{aligned} \tag{17}$$

where $Y_0 = \frac{4\pi\sin\varphi_{\text{ref}}}{c}f_c$. When the phase error $\Delta\Phi(X,Y)$ is greater than $\pi/4$, it indicates that the APE cannot be simply regarded as a 1-D phase error, and the 2-D effect of the error should be considered separately.

In [34], a compensation method based on the correlation of APE, residual RCM, and residual 2-D phase error is proposed. By 2-D representation of 1-D APE and residual RCM, the residual 2-D phase errors are compensated. The corresponding relationship between residual RCM and residual 2-D phase error

is expressed as follows:

$$\Phi(X,Y) = XY \int \frac{\phi_1\left(\frac{Y_0}{Y}X\right)}{X^2} dX + CX. \tag{18}$$

Equation (18) involves an integral with the azimuth time as the denominator, which causes the computed results to be significantly affected by the residual RCM ϕ_1 when calculating at $X = 0$ and beyond. Therefore, the key to deriving 2-D errors using this equation lies in the accuracy of the residual RCM estimation.

However, in the context of high-resolution applications of THz SAR systems, the influence of RCM is magnified, which affects the accuracy of conventional RCM estimation methods and increases error compensation difficulty. If the main compensation operation is carried out before the error is converted into two dimensions by PFA, it not only reduces the computational complexity and improves the robustness but also diminishes the error's influence of the subsequent autofocus algorithms, thus enhancing the optimization effect of the autofocus algorithms.

III. Motion Error Compensation

Motion error of the radar platform will cause two kinds of effects on echo signal: APE and residual RCM. The former causes azimuth defocusing, while the latter causes image distortion. These two classes of errors exhibit a simple linear relationship, where the APE is the product of $4\pi/\lambda$ and the residual RCM. Therefore, estimating either of these two types of errors can compensate for the motion error of the entire platform. The commonly used methods to compensate APE include the phase gradient algorithm [35], MCA [36], and minimum entropy algorithm [37], which are all 1-D autofocus algorithms. However, autofocus algorithms are postprocessing technology, which needs to process a certain quality of image data. And when the RCM exceeds the range resolution, the estimation accuracy of autofocus algorithm decreases significantly.

One way to meet the autofocus requirement is to reduce the range resolution of range-compressed data, and then estimate the APE based on these reduced resolution data. On this basis, the residual RCM is calculated to compensate. However, because this method relies on low-resolution data to estimate APE, its accuracy is limited, and it is difficult to meet the requirements of a high-resolution THz SAR system.

As can be seen from the analysis in Section II, the 2-D coupling of useful information in the frequency-modulated signal still exists before the Keystone transformation during the polar coordinate format resampling process. The error component is not converted to the 2-D domain. The estimation and compensation of the original error can significantly reduce the influence of the error introduced by PFA in the 2-D transformation process.

Therefore, the estimation of residual RCM is conducted before the Keystone transformation. Then, the total translation error of this stage is calculated according to the estimated residual RCM, and the initial compensation is realized. Since PFA processing has not yet been completed at this stage, estimating residual RCM through frequency fitting is a strategy worth considering to maintain the original signal structure. In addition, the error estimation method used in coarse compensation is based on 1-D error. Before PFA, the signal appears in the form of 2-D coupling, and the accuracy of 1-D error estimation method will be insufficient.

First, 2-D FFT is applied to transform the signal from wavenumber domain to image domain so as to facilitate the selection of characteristic points. Fig. 3 shows the flowchart of the coarse estimation process, which contains the selection of characteristic points. The following is a detailed error estimation process based on the reference point.

According to (8), for the selected target reference point (x_p, y_p), the signals of any two adjacent azimuth pulses t_n and t_{n+1} can be expressed as follows:

$$\begin{aligned} S_n(f_r) &= A \cdot \exp\left\{ j \frac{4\pi (f_c + f_r)\sin\varphi_{\text{ref}}}{c} \right. \\ &\qquad \left. [x_p \Omega t_n + y_p + \eta(t_n)] \right\} \\ S_{n+1}(f_r) &= A \cdot \exp\left\{ j \frac{4\pi (f_c + f_r)\sin\varphi_{\text{ref}}}{c} \right. \\ &\qquad \left. [x_p \Omega t_{n+1} + y_p + \eta(t_{n+1})] \right\}. \end{aligned} \tag{19}$$

Multiply the two expressions in (19) by conjugation to get the following phase:

$$\begin{aligned} \Phi\left[S_{n+1}(f_r) \cdot S_n^*(f_r)\right] &= \frac{4\pi (f_c + f_r)\sin\varphi_{\text{ref}}}{c} \\ &\qquad (x_p \Omega dt + d\eta) \end{aligned} \tag{20}$$

where $dt = t_{n+1} - t_n$; $d\eta = \eta(t_{n+1}) - \eta(t_n)$ and is a term needed in motion error compensation. It can be seen that the term in (20) associated with f_c is a constant, and the only variable is the range frequency f_r.

Substitute the following transformations into (20):

$$\begin{aligned} a &= \frac{4\pi \sin\varphi_{\text{ref}}}{c} (x_p \Omega dt + d\eta) \\ b &= \frac{4\pi f_c \sin\varphi_{\text{ref}}}{c} (x_p \Omega dt + d\eta). \end{aligned} \tag{21}$$

Then, (20) can be simplified to the following form:

$$\Phi(f_r) = a f_r + b \tag{22}$$

where a represents the slope of the linear function and can be estimated by fitting the phase difference curve $\Phi(f_r)$ using the least squares method. In the process of selecting the target reference point, the target information x_p is known. After obtaining a, the term $\frac{4\pi \sin\varphi_{\text{ref}}}{c} x_p \Omega dt$ in a can be eliminated based on the target information x_p, thereby deriving the differential error term $d\eta$ along the azimuth direction.

In practical applications of SAR systems, there is typically a significant amount of noise and clutter. This interference leads to unknown differences between adjacent azimuth pulses in (19), thereby disrupting the accuracy of the fitting estimation. According to the analysis of Pu et al. [38], the difference between adjacent azimuth pulses in (19) can be divided into two components: the macrosimilarity term corresponding to

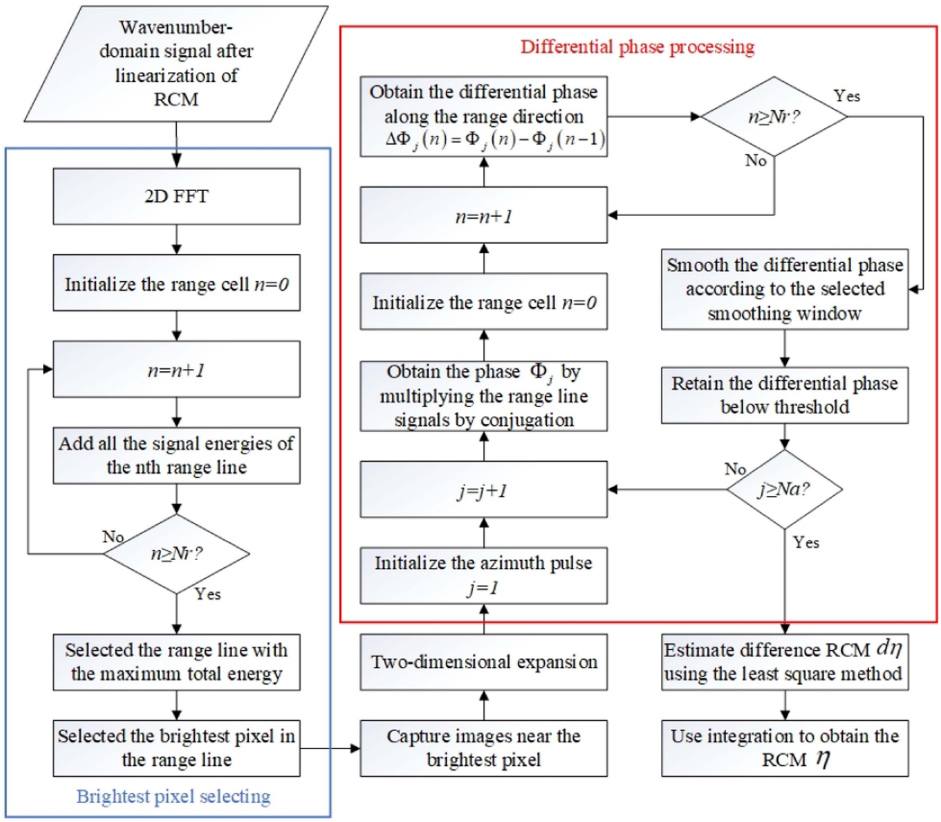

Fig. 3. Flowchart of coarse estimation.

the low-frequency component of the spectrum and the detailed difference term corresponding to the high-frequency component of the spectrum. The low-frequency component is similar to the ideal phase curve and the data part required for the above fitting method. By removing the high-frequency component from the data, the differential error term $d\eta$ can be fitted more accurately using the low-frequency information. The specific acquisition process is as follows.

1) *Obtain the Differential Term:* Represent the phase $\Phi(f_r)$ as its discrete version $\Phi(n)$, $n\epsilon(0, N_r - 1)$. Obtain the differential term $\Delta\Phi(n)$ of $\Phi(n)$ as follows:

$$\Delta\Phi\left(n\right) = \Phi\left(n\right) - \Phi\left(n-1\right). \tag{23}$$

2) *Smooth the Differential Term:* Apply the average filter to smooth the differential term $\Delta\Phi(n)$ as follows:

$$\varsigma\left(n\right) = \sum_{i\epsilon\left(-\frac{W}{2},\frac{W}{2}-1\right)} \Delta\Phi\left(n+i\right)/W \tag{24}$$

where W indicates the selected smooth window width.

3) *Search the Low-Frequency Region:* Set a threshold ς_{th} and perform a peak search on $\varsigma(n)$ starting from the central zero frequency. Stop the search when the peak value exceeds the threshold ς_{th}. Specify the region covered by the search as a low-frequency region for fitting.

After obtaining a more accurate differential error term $d\eta$ through low-frequency fitting, the error $\eta(t)$ can be obtained by term-by-term integration, as shown in the following equation:

$$\hat{\eta}\ (k) = \sum_{i=1}^{k} d\eta\,(i)\quad k\ =\ 1, 2, \ldots, N_a. \tag{25}$$

Subsequently, the coarse-compensation term $H(t)$ can be constructed as follows:

$$H\ \ (t) = \exp\left[-j\frac{4\pi\left(f_c + f_r\right)\sin\varphi_{\text{ref}}}{c}\hat{\eta}\,(t)\right] \tag{26}$$

where $\hat{\eta}(k) = \hat{\eta}(t)|_{t=k\cdot\text{PRT}}$ and PRT is the pulse repetition time.

Therefore, the coarse compensation of the echo signal is completed by multiplying (26) with (8). And the coarse-compensated signal $S_{c1}(t, f_r)$ can be expressed as

$$\begin{aligned} S_{c1}\left(t, f_r\right) &= S_{A1}\left(t, f_r\right) * H\left(t\right) \\ &= A \cdot \exp\left\{j\frac{4\pi\left(f_c + f_r\right)\sin\varphi_{\text{ref}}}{c}\right. \\ &\quad \left.\left[x_p\Omega t + y_p + dR\left(t\right)\right]\right\} \end{aligned} \tag{27}$$

where $dR(t) = \eta(t) - \hat{\eta}(t)$ is the residual error after coarse compensation.

The above processing eliminates a significant portion of the 1-D motion errors while maintaining the original model structure of the signal, which is conducive to the subsequent PFA processing operations. Therefore, performing the Keystone

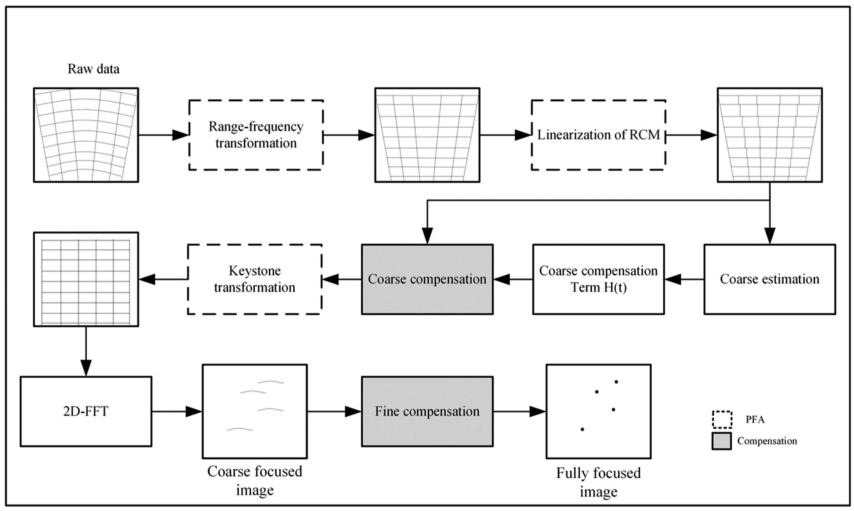

Fig. 4. Flowchart of the proposed method.

transformation on the signal $S_{c1}(t, f_r)$ in (27) completes the entire process of PFA. And the 2-D decoupling of the signal is as follows:

$$S_{c2}(t, f_r) = A \cdot \exp\left\{ j \frac{4\pi \sin\varphi_{\text{ref}}}{c} \left[f_c x_p \Omega t + (f_c + f_r) y_p + (f_c + f_r) dR\left(\frac{f_c}{f_c + f_r} t \right) \right] \right\}. \tag{28}$$

At this time, if the FFT is directly applied to (28), the compressed image can be obtained. However, the presence of residual error $dR(t)$ will cause some defocusing in the image. Therefore, after completing the Keystone transformation, it is also necessary to use an autofocus algorithm, such as MCA, for fine compensation of errors.

The logic of MCA is based on the optimization of the overall image quality, which sometimes leads to an interruption of the signal's prior structure, making the remaining step of PFA, the "Keystone transformation" no longer accurate. Therefore, after the Keystone transformation, it is planned to use MCA for fine compensation. This is the final step in obtaining the high-quality SAR image.

On the basis of a comprehensive analysis of error estimation and compensation processing, the overall flowchart of the proposed method is shown in Fig. 4. It is worth noting that the coarse-compensation process of the proposed method can be iterated until the residual RCM does not affect the image quality.

IV. Experimental Results

A. Processing of the Simulation Data

The key of the proposed method is the change of residual phase error before and after resampling of polar format. Therefore, it is very important to verify the necessity and rationality of the proposed method through the processing of simulation data. At the same time, after using PFA to process the echo data, we choose the traditional autofocus methods, such as MCA and rRCMC+MCA to estimate and compensate the error of the data so as to compare with our method. The rRCMC described here is not a simple residual RCM estimation and compensation. Instead, the residual RCM is estimated first, and then the overall phase error is calculated by the linear relationship between residual RCM and APE. The main parameters of THz SAR system used in this simulation are shown in Table I.

TABLE I
Parameters of the Simulation System

Parameters	Value
Carrier frequency	216 GHz
Bandwidth	5 GHz
Range resolution	0.0532 m
Azimuth resolution	0.0298 m
Slant range	1500 m
Platform speed	80 m/s
Elevation angle	45°

Nine point targets are positioned in the scene for imaging. The radar works in spotlight mode, producing error-free PFA-focused images, as shown in Fig. 5. To simulate airborne SAR imaging in real scenarios, the nonlinear platform translation errors are introduced into the simulated echo data. The phase errors caused by these translation errors are depicted in blue line of Fig. 6(a). Notably, the phase errors represent 1-D motion errors that exist prior to PFA processing. After the signal is decoupled by the PFA, these 1-D phase errors undergo a 2-D coupling transformation.

According to the analysis of the 2-D coupling error of PFA in Section III, the 2-D coupling error after PFA processing can be calculated, and the results are shown in Fig. 7(a). Combined with the parameters in Table I, the 2-D differential value of the phase error is calculated by (19), which is about ± 55 rad, as shown in Fig. 7(b). Meanwhile, the contours of $\pm\pi/4$ and $\pm\pi/2$ are marked with red and blue lines, respectively. It can be seen that most of these error values exceed the tolerance range

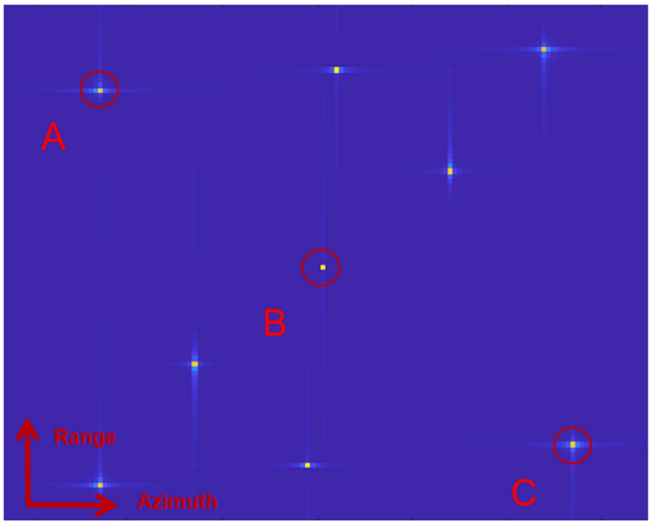

Fig. 5. Error-free simulation images generated by PFA.

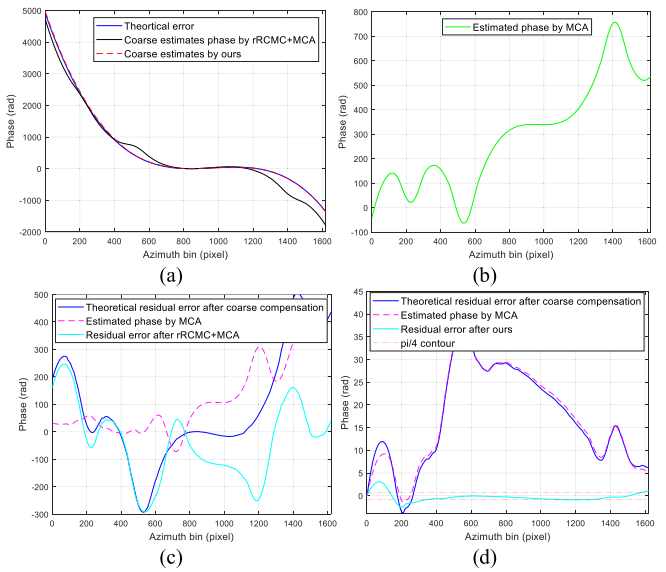

Fig. 6. Various phase errors of a simulation experiment. (a) Initial global phase error and coarse-compensation estimated phase. (b) Estimated phase of MCA. (c) Residual phase error and estimated phase of rRCMC+MCA after coarse compensation. (d) Residual phase error and estimated phase of our method after coarse compensation.

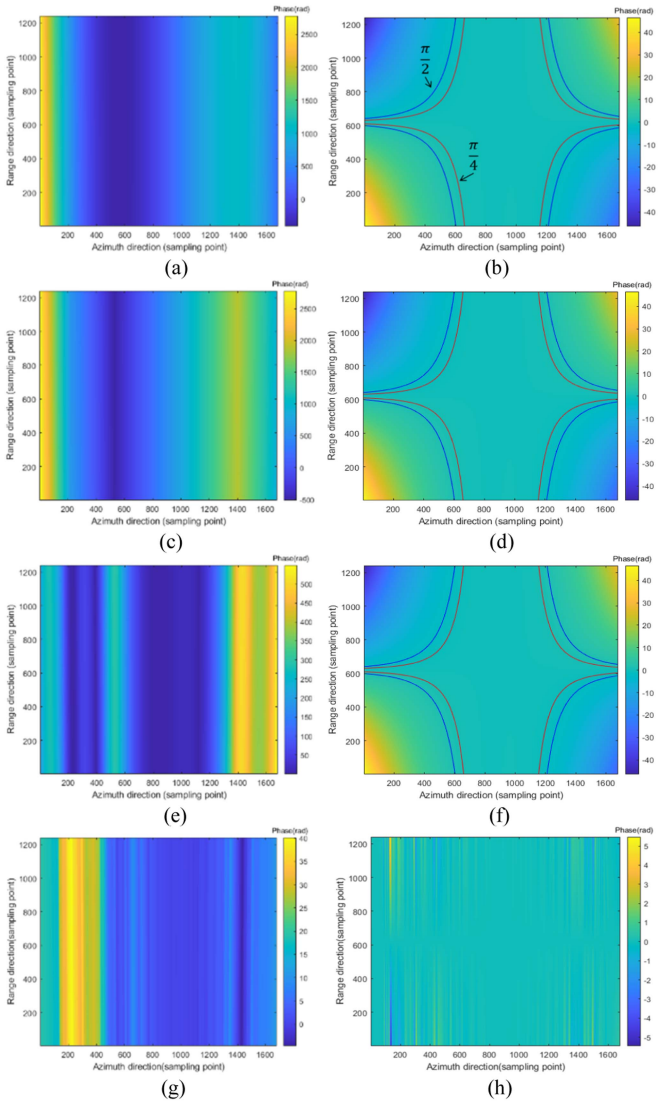

Fig. 7. Two-dimensional phase error of simulation experiment. (a) Uncompensated phase error of PFA. (c), (e), and (g) Remaining 2-D phase errors by the initial compensation of three methods (MCA, rRCMC+MCA, and our method). (b), (d), (f), and (h) Additional phase errors introduced by PFA of different methods (PFA, MCA, rRCMC+MCA, and our method).

of $\pm\pi/4$. At this time, the influence of 2-D coupling cannot be ignored, which will aggravate the degradation of image quality and affect the effectiveness of error compensation processing. After PFA imaging without error compensation, the image is shown in Fig. 8(a). As can be seen from Fig. 8(a), the phase error will affect the image quality, resulting in severe azimuth ghosting, image warping, and range defocus.

First, let us look at the performance of MCA approach. The APE estimated by this method is shown in Fig. 6(b). As the carrier frequency increases, the phase error is amplified, causing the phase error between the two adjacent azimuth pulses to sometimes exceed $\pm\pi$. As a result, the results of autofocus algorithm based on phase estimation fluctuate greatly, and the accuracy of the method is reduced. After compensating the signal with the estimated APE, the remaining 2-D error is shown in Fig. 7(c). Obviously, in high carrier frequency and high-resolution THz SAR system, the direct compensation effect of MCA is not ideal, resulting in large uncompensated errors in the signal. In addition, since MCA only compensates for 1-D errors, the problem of introducing 2-D differential errors in PFA [as shown in Fig. 7(d)] remains unresolved. The final compensation image is shown in Fig. 8(b), clearly showing 2-D defocusing and RCM in space. There is no doubt that uncompensated APE and 2-D differential errors introduced by PFA [as shown in Fig. 7(c) and (d)] are the main causes of 2-D defocusing of images. The existence of RCM shows that residual RCMC is an indispensable aspect in THz SAR system, and its influence cannot be ignored.

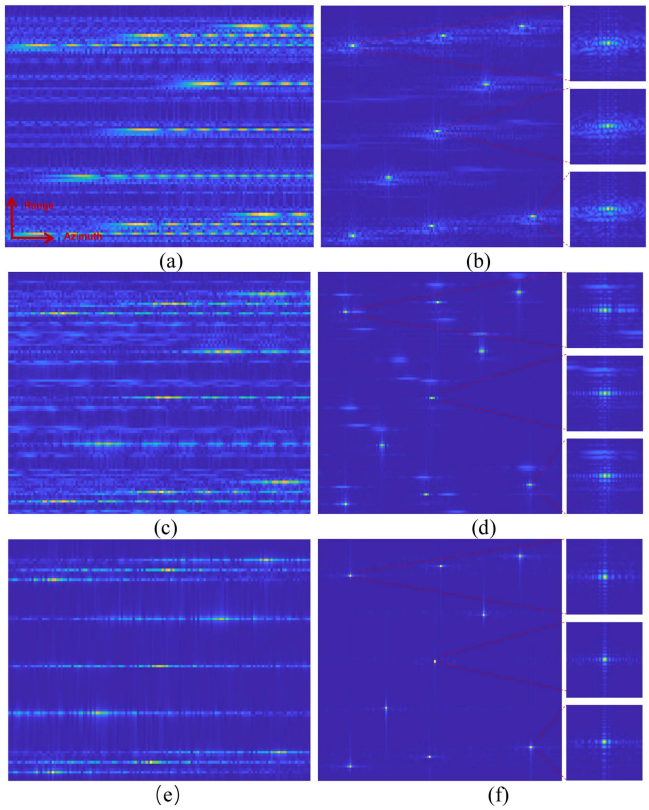

Fig. 8. Image of simulation experiment. (a) Original image by PFA. (b) Image compensated by MCA. (c) Coarse-compensated image by rRCMC+MCA. (d) Image compensated by rRCMC+MCA. (e) Coarse-compensated image by our method. (f) Image compensated by our method.

In light of the above issues, the second control group, rRCMC+MCA, introduces a coarse-compensation step before autofocus processing and estimates and corrects the overall phase error by low-frequency fitting. The estimated phase of this step is shown by the black line in Fig. 6(a), and the theoretical residual phase after coarse compensation is shown by the blue line in Fig. 6(c). We can see that the coarse-compensation effect of error is not perfect, and there are still many residual errors that affect the image quality. Then, compensating the signal using the estimated phase shown by black line of Fig. 6(a) yields a residual 2-D error, as depicted in Fig. 7(e). The differential value of this 2-D error, relative to the error at $f_r = 0$, is illustrated in Fig. 7(f). The 2-D error introduced by the PFA has not been eliminated, which still results in the 2-D defocusing of the image. Fig. 8(c) shows the coarse-compensation image, which has a certain compensation effect in both range and azimuth dimension compared with Fig. 8(a), but there is still a certain gap compared with the compensated image of MCA.

The residual error after coarse compensation can be further estimated by MCA, and the autofocus estimation results are shown by the pink line in Fig. 6(c). We find that the MCA estimates differ greatly from the theoretical residuals, which results in a large residual phase error even after autofocusing, as shown in cyan in Fig. 6(c). This is because after the PFA Keystone transformation, the phase error is changed from 1-D to 2-D, and MCA fails. Finally, the final compensation image is shown in Fig. 8(d). Compared with MCA, the coarse-compensation step of rRCMC+MCA can optimize the 2-D defocusing phenomenon in the image and eliminate a part of the range migration, and get a better focusing effect. However, it is worth noting that there is still some 2-D defocusing in Fig. 7(d), which confirms the existence of the above 2-D error.

Compared with the above two methods, it can be seen that coarse compensation can significantly reduce the phase error and improve the focusing quality of the image. Therefore, the two-step method is more effective for error estimation and compensation of THz SAR system.

Our proposed method is based on the analysis of PFA signal transformation model, using a low-frequency fitting approach before PFA Keystone transformation to estimate the residual RCM. Then, combined with the linear relationship between residual RCM and APE, the total phase error on the space is derived and roughly compensated. The resulting APE is shown by the red line in Fig. 6(a). The estimated error in Fig. 6(a) is very close to the theoretical error. This is because, at this stage, PFA has not yet caused 2-D coupling of signal errors, making the error estimation accuracy higher than the estimation after PFA Keystone transformation processing. Therefore, after high-precision coarse compensation, the residual phase error is significantly reduced, as shown in the blue line in Fig. 6(d). At this point, the theoretical residual phase error is one order of magnitude smaller than that of the rRCMC+MCA method, which shows that the error estimation and compensation before the Keystone transformation are effective.

The 2-D error after PFA can be obtained by calculating the residual error after coarse compensation, as shown in Fig. 7(g). And Fig. 7(h) gives the differential value of this 2-D error. By comparing Fig. 7(b), (d), and (f), it can be seen that the 2-D error differential originally distributed in space has been eliminated to a large extent. This indicates that the error of 2-D coupling no longer has a significant effect. At this time, Fig. 8(e) gives the image after the coarse compensation of our method. Compared with the coarse-compensation image obtained by rRCMC+MCA, it can be seen that our method can perform more accurate coarse-compensation processing and the coarse-compensation image has a more effective optimization effect in both dimensions. From the above analysis, it can be seen that the residual error after coarse compensation can be estimated as a 1-D error without significantly affecting the image quality. At this time, the result of error estimation using MCA is shown in the pink line in Fig. 6(d), which matches well with the theoretical residual. This makes the residual error after further fine compensation very small, as shown in the cyan line in Fig. 6(d). It is evident that the remaining error at this stage is mostly within the tolerable range of $\pm\pi/4$ and will not affect the image quality. Fig. 8(f) shows the final compensation image, where the RCM no longer exists and the 2-D defocusing phenomenon is completely eliminated. Compared with the results of the previous two methods, the image processed by our method has a higher overall quality.

Fig. 9 shows the range-compressed images of the three compensation methods. It can be seen from the comparison that the

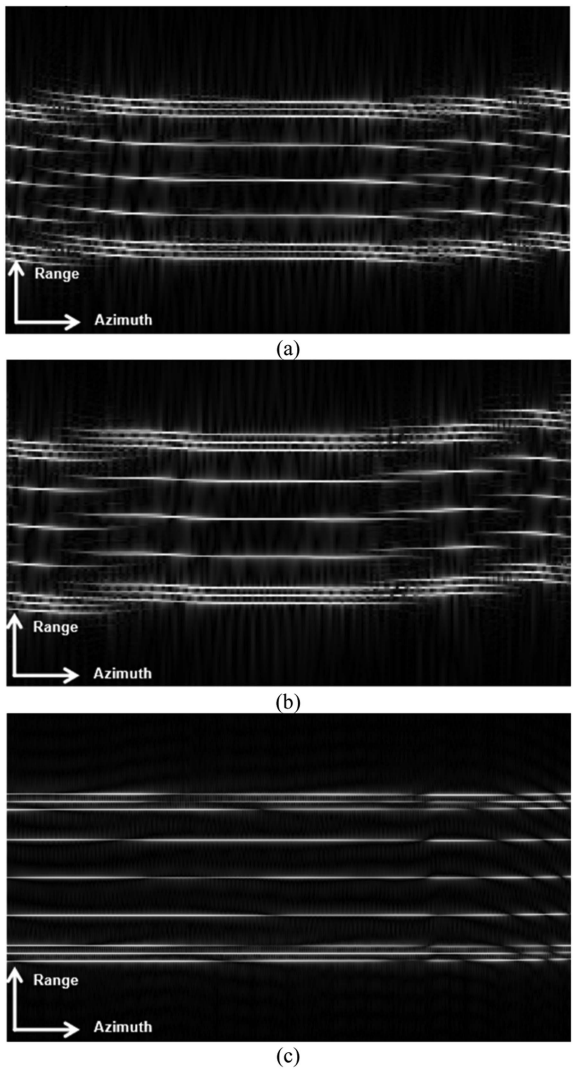

Fig. 9. Range-compressed image. (a) MCA. (b) rRCMC+MCA. (c) Ours.

range-compressed image compensated by MCA in Fig. 9(a) has obvious RCM. After rRCMC+MCA processing, the bending at both ends of Fig. 9(b) is corrected to a certain extent, but the same target is not corrected to the same range cell, resulting in errors in the focused energy points in the compressed image. The range-compressed image processed by our proposed method not only has no obvious bending at both ends but also ensures that the target can appear in the correct range cell.

In order to quantitatively evaluate the performance of different methods, three-point targets, as marked red in Fig. 5, are selected for quantitative analysis, and the profile results are shown in Fig. 10. By comparing the analysis results of the three methods, it can be seen that the three methods are ideal in the range direction of main lobe compression. And the impulse response width (IRW) of the three methods in the range direction is very close to the theoretical value of 0.0530 m. But the three methods differ in other ways. First, MCA has the worst azimuth main lobe compression, and its IRW is 0.0580 m, much higher than the theoretical value of 0.0298 m. In addition, the 2-D sidelobe

TABLE II
PARAMETERS OF AIRBORNE SPOTLIGHT THZ SAR SYSTEM

Parameters	Value
Carrier frequency	216 GHz
Bandwidth	1 GHz
Range resolution	0.1496 m
Azimuth resolution	0.0806 m
Slant range	1000 m
Platform speed	28.72 m/s
Elevation angle	48°

effect of MCA is not good, which affects the image quality. Second, the overall situation of rRCMC+MCA is better than that of MCA. It can be seen from Fig. 10 that the widening of the main lobe in the azimuth direction is significantly reduced. And its IRW drops to about 0.0370 m. The range-dimensional sidelobe is also well suppressed. However, this method still has some shortcomings. For example, there is still a −12 dB large companion lobe in the azimuth profile of point A in Fig. 10(d). Furthermore, in Fig. 10(a)–(c), the range profile has a −11 dB sidelobe. This shows that the error estimation of the method is not accurate, which leads to the phantom of the target in the image. Finally, our approach is superior to MCA and rRCMC+MCA in both dimensions. The azimuth IRW is 0.0351 m, which is very close to the ideal value. The peak sidelobe ratio of range dimension is also the best. The azimuthal peak sidelobe ratio is slightly worse than rRCMC+MCA, but this is mainly due to the widening of the main lobe of rRCMC+MCA to absorb the first sidelobe. In summary, the performance of the proposed method is obviously superior to the other two methods.

B. Experimental Verification

In this section, the real raw echo data collected by airborne THz SAR system is used to verify the validity of the proposed compensation method. The data are acquired by the 0.22-THz airborne spotlight SAR system, developed by the 14th Research Institute of China Electronics Technology Group Corporation. The target scene is an airport runway with three ground corner reflectors, and the range and azimuth dimensions of the imaging scene are 96.0 m and 52.5 m, respectively. Table II gives the radar system parameters.

First, PFA is used to directly process the measured echo data without any motion error compensation. Fig. 11(a) shows the imaging results. The vertical and horizontal directions of SAR images represent the range and azimuth dimension, respectively. As can be seen from Fig. 11(a), THz SAR image has obvious 2-D defocusing, distortion, and ghosting phenomena. This shows that PFA processing signal has an obvious 2-D error, which affects the image quality. Compared with Fig. 11(a), the image quality after MCA compensation is improved. This shows that MCA method can estimate and compensate a part of the error. However, because the error after PFA has the characteristics of 2-D space variation, even after MCA method estimation and compensation, there is still a lot of error interference. As a result, the imaging results are still heavily defocused. Fig. 11(c) is the imaging result of rRCMC+MCA. In Fig. 11(c), after PFA, the

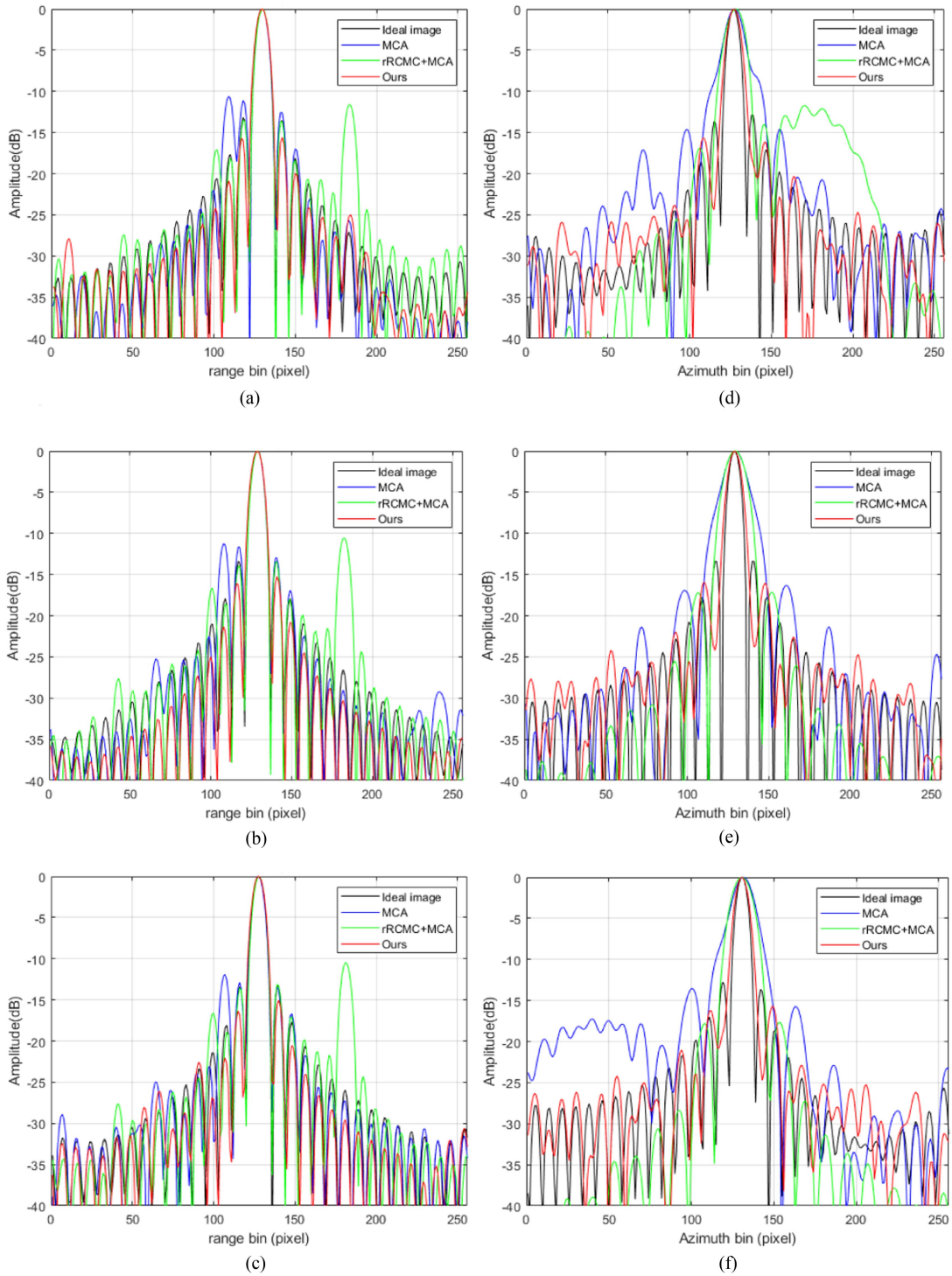

Fig. 10. Performance evaluation of point targets for red circled in Fig. 5. (a) Range profile of point target A. (b) Range profile of point target B. (c) Range profile of point target C. (d) Azimuth profile of point target A. (e) Azimuth profile of point target B. (f) Azimuth profile of point target C.

residual RCM is compensated and the phase errors are resolved using MCA. The defocusing and ghosting problems caused by residual RCM and APE are significantly improved, and point targets, road conditions, and arrow signs in the image can be clearly observed. However, the resampling of the polar coordinate format converts the original 1-D error into a 2-D error, thus reducing the effect of autofocus. Despite the iterative optimization of the error estimation, the reduction of autofocus results in a decrease in the overall quality of the image scene. Fig. 11(d) is the imaging result of our proposed method. In Fig. 11(d), our proposed method achieves clarity and compression of the point targets while maintaining the image quality of the surrounding environment in the image. Road conditions and arrow signs are clearly visible.

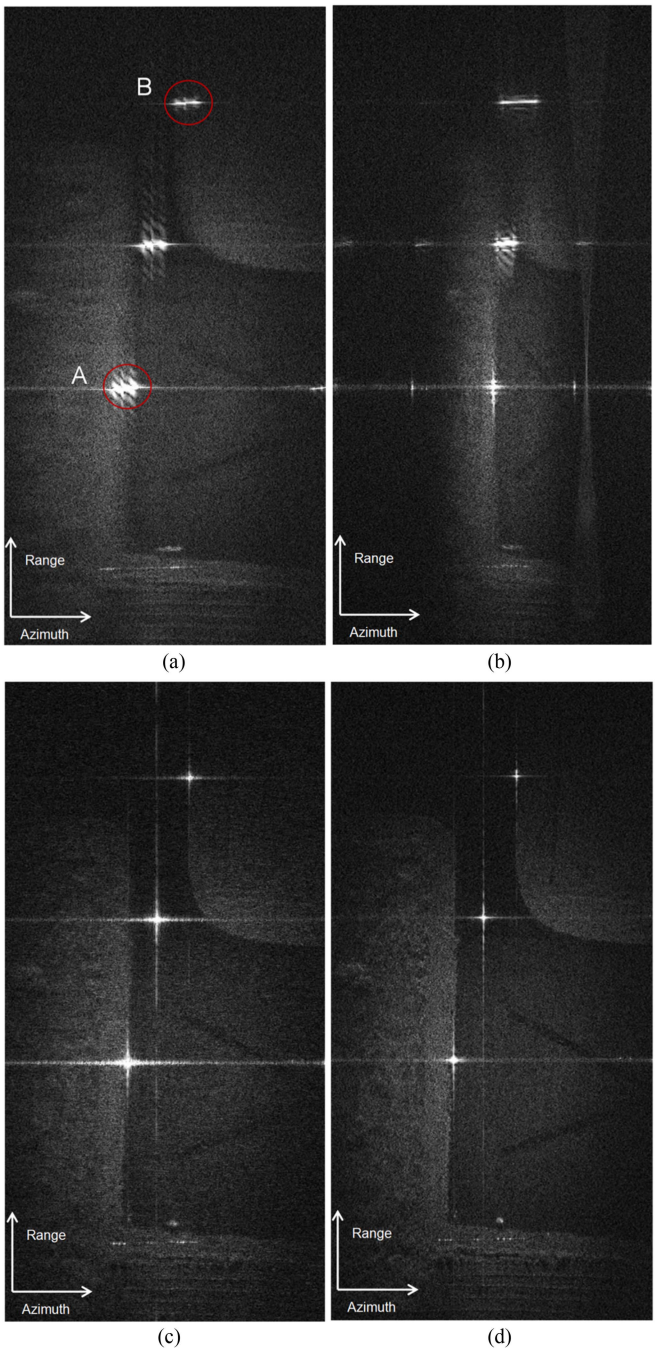

Fig. 11. Image of the measured data with different motion compensation methods. (a) No compensation. (b) MCA. (c) rRCMC+MCA. (d) Our method.

In order to more clearly represent the experimental process, the error estimation results are given in Fig. 12. Fig. 12(a) shows the residual RCM estimated by rRCMC+MCA and our method. The phase of coarse compensation is obtained based on the linear relationship between residual RCM and APE. Fig. 12(b) shows the total phase errors estimated and compensated by the three methods. Since the actual error is unknown, it can be seen from the imaging results that the estimation results of the proposed method should be the best.

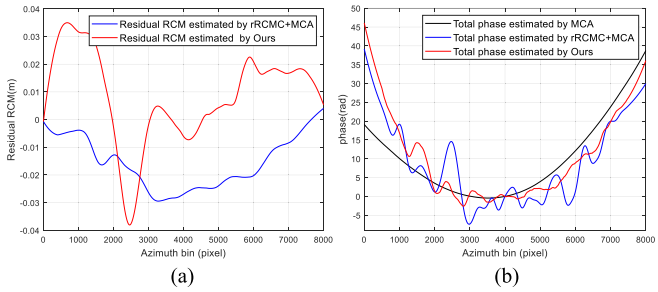

Fig. 12. Error estimation results of the measured data. (a) Estimated residual RCM. (b) Estimated total phase.

For quantitative analysis of the measurement experiment, two point targets in these images are analyzed next. The selected point targets have been marked in Fig. 11, and the analysis results are shown in Fig. 13. As can be seen from Fig. 13, for the uncompensated PFA image, the azimuth dimension is severely defocused. This is because the motion error in the signal seriously affects the image quality. The numerical expression of this effect is that the azimuth IRW of the image point target is 0.3483 m and 0.3799 m, respectively, which is significantly different from the ideal value of 0.0806 m. Moreover, the sidelobe of point B reaches −15 to −20 dB in the range dimension, which is more significant than that of point A and other methods. This is because the image has not been compensated at this time, and there is a 2-D space–time error in the signal, which makes the performance of the point target in the image inconsistent.

The image compensated by MCA has good azimuth-focusing performance at point A, and its azimuth IRW is 0.0985 m and much better than that without compensation. However, this method does not get a similar compensation effect at point B. The azimuth profile of point B shows that the point has not completed azimuth focusing, and its azimuth IRW is 0.3517 m. We can see that the azimuth IRW before and after compensation is not much different. And the range profile of point B is worse than that of PFA image. This is because the image error after PFA processing has 2-D coupling. Although the simple azimuth-dimension MCA can optimize the overall image quality, the optimization effect for different areas of the image is not consistent.

In the azimuth direction, the performance of rRCMC+MCA is more stable. It can be seen from the profile that two points A and B have relatively consistent compensation conditions, and their azimuth IRWs are 0.086 8 m and 0.0861 m, respectively. At the same time, the focusing effect of range dimension is also very good, of which point B has the best focusing effect. Its range Peak Side Lobe Ratio (PSLR) reaches −13 dB. This is because the application of rRCMC eliminates the residual RCM in the signal, thereby improving the optimization efficiency of MCA.

The processing effect of our method is better than the previous two methods. From the azimuth profile of the targets in Fig. 13(b) and (d), it can be seen that the focusing effect of point A is not much different from MCA, while the focusing effect of point B is significantly better than the first two methods. In addition, the overall optimization effect of our method is consistent. The azimuth-dimension IRW of points A and B is

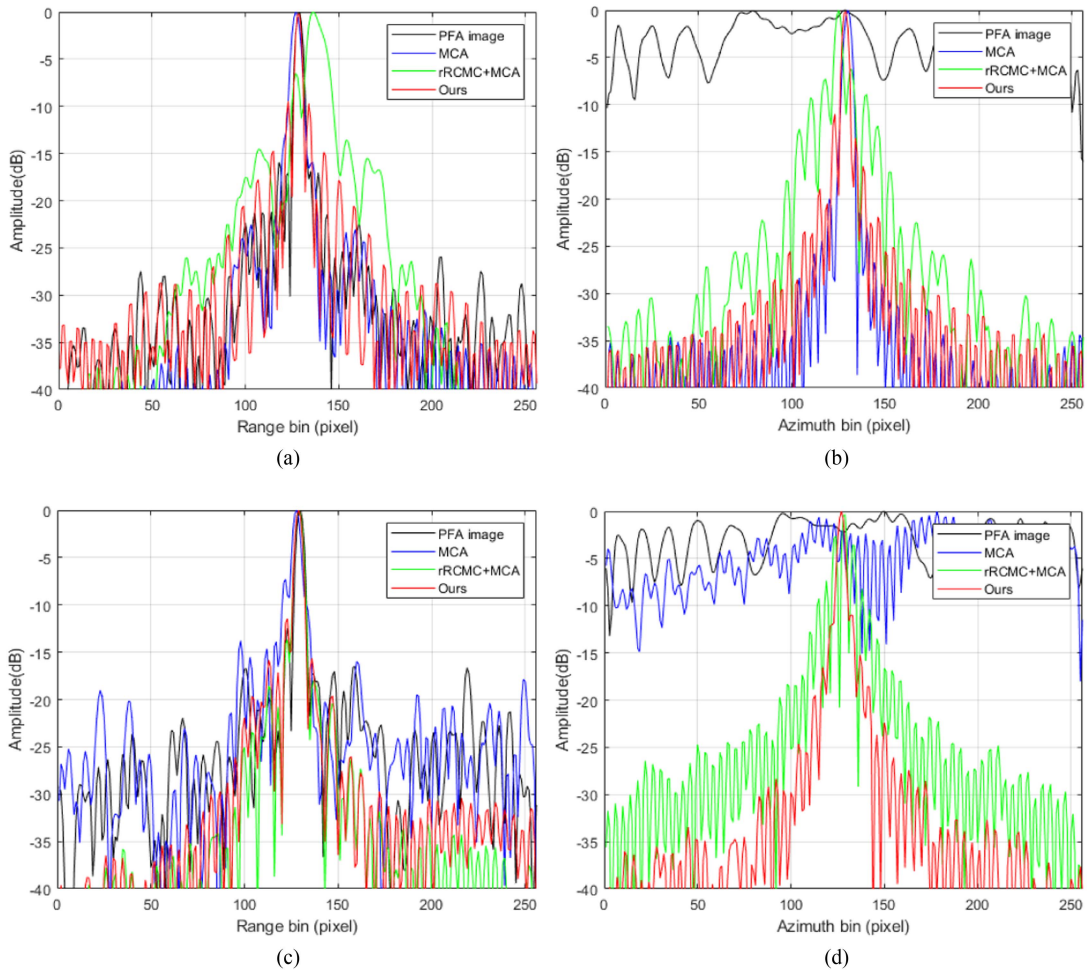

Fig. 13. Profile of marked points. (a) Range profile of marked point A. (b) Azimuth profile of marked point A. (c) Range profile of marked point B. (d) Azimuth profile of marked point B.

TABLE III
NUMERICAL EVALUATION OF IMAGE QUALITY

Image	PFA	MCA	rRCMC+MCA	Ours
Entropy Value	10.1090	8.4836	7.9889	6.3127
Contrast value	5.5009	10.5626	11.1812	12.4958

0.0815 m and 0.0821 m, respectively, which accords with the theoretical IRW value of 0.0806 m. From the observation of the two profiles of the range dimension, although the sidelobe elimination effect of our method is not the best at points A and B, the overall performance is the most stable. It is because our method performs coarse compensation before PFA Keystone transformation, which greatly eliminates the 2-D coupling effect of PFA on errors.

In order to more intuitively understand the compensation effect of the above methods, image entropy and contrast are used to evaluate the images before and after compensation, as shown in Table III. The entropy and contrast values of the uncompensated PFA image are 10.1090 and 5.5009. After MCA compensation, the image entropy and contrast values reach to 8.4836 and 10.5626. Compared with uncompensated PFA image, MCA-compensated image has great improvement. Compared with MCA, rRCMC+MCA also has a certain improvement in image entropy and contrast, which are 7.9889 and 11.1812, respectively. Although the optimization effect of MCA is better than rRCMC+MCA in some areas of point-target analysis, the overall optimization effect is inferior to rRCMC+MCA due to the limitation of 1-D autofocusing compensation. Finally, the image entropy and contrast values after compensation with our proposed method are 6.3127 and 12.4958, respectively, which are obviously higher than the image quality of the other two comparison methods. In general, our method has a good compensation effect for both the single point target and the whole image, and is an effective method for motion error compensation.

The three different methods compared in this article all use residual RCMC and/or MCA for processing. However, the process is different for three methods. This makes the focusing quality of the images that MCA needs to process different, which affects the number of iterations required to converge the results. Therefore, it is difficult to compare the processing efficiency of different methods in terms of complexity. In the following, the running time of different methods is compared to prove the efficiency of the proposed method.

The running time of the three methods from PFA processing to the final image are 35.7499 s, 34.2328 s, and 24.6534 s, respectively. At the same time, the MCA iterations of the three methods are 42, 36, and 21 times, respectively. Compared with MCA method, rRCMC+MCA method and the proposed method reduce the number of iterations of autofocus by coarse compensation. Compared with rRCMC+MCA method, the proposed method has smaller errors and fewer iterations after coarse compensation, which improves the processing efficiency. It should be noted that the running time and number of iterations of the above three methods are based on specific imaging data, and the running time and number of iterations obtained by processing different data will be slightly different.

V. Discussion

THz SAR has more accurate and in-depth requirements for motion error compensation. PFA introduces a 2-D coupled error to the existing motion error while decoupling the signal.

Most of the existing methods to solve this problem are to calculate and eliminate this part of the error after PFA. Although this way can also get the accurate compensation terms, deriving the 2-D form of compensation terms from the estimated error value always increases the overall calculation amount of the method. If the unchanged error is compensated before PFA, then the 2-D error introduced by PFA will be reduced accordingly, and even its influence can be directly ignored. After the whole transformation process of the signal is clearly defined, the compensation idea does not need additional derivation calculation and reduces the overall calculation amount.

In simulation and real data processing experiments, we first divide PFA 2-D resampling into three steps. After completing the first two steps that do not involve 2-D transformation, the echo signal is divided into two parts: low frequency and high frequency so as to avoid the influence of scene clutter on error estimation and obtain effective information. The RCM term is estimated by the least square method. According to the linear relationship between the residual RCM and the APE, the coarse-compensation term is constructed. After the coarse compensation is completed, the third step of PFA Keystone transformation is carried out, and the polar format image is obtained by 2-D FFT. Finally, MCA is used to further improve the image quality. Experimental results show the effectiveness of the proposed method.

In addition, we also analyze the PFA imaging scene limit, the error processing limit, and the 2-D spatial variation of motion error of the proposed method. Based on the analysis of system parameters and actual error fluctuations, we ultimately decided not to consider these effects. The correlation analysis is given as follows.

1) PFA resampling of 2-D signals is performed based on the plane wave hypothesis. This will introduce additional phase errors and image distortion problems. When the image scene is large enough, it will fail. At present, the plane wave hypothesis of spotlight SAR is established in the $\pi/2$ region of $2\rho_a\sqrt{r_a/\lambda}$ and $\pi/4$ region of $\rho_a\sqrt{2r_a/\lambda}$, where ρ_a is the azimuth resolution and r_a is the radius of the imaging scene. These problems have been studied in detail in [32], and the proposed compensation strategy can be combined with our proposed method if needed.

In addition, THz SAR has a smaller beamwidth, making its imaging scene area smaller. For example, the measured data used in this article are taken from a region of 52.5 m$*$96.0 m, which is less than the $\pi/4$ allowable limit of 67.6 m radius.

Therefore, the image distortion problem of PFA is not considered in this article.

2) For motion error compensation methods, the region of motion errors that can be handled is a problem to be considered. Excessive motion error will greatly reduce the accuracy of the compensation method. The motion error compensation is a systematic process. In the THz SAR imaging and error compensation method proposed in this article, the application range of motion error is discussed from two aspects.

On the one hand, the existing DGPS/IMU can control the error in the order of centimeters during the initial correction so as to ensure the smooth operation of the compensation method. On the other hand, the cross-correlation principle is used for estimation in the coarse-compensation step, and MCA is used for autofocus in the fine compensation step. These two methods have a large tolerance range in optimizing image quality. Combined with the above two points, the proposed method in this article is suitable for most of the existing motion error ranges to a certain extent.

At present, based on the measured data of a 220-GHz airborne spotlight SAR system, the error processing effect of the proposed method is tested, and satisfactory results are obtained. But unfortunately, due to the immaturity of THz SAR system and the lack of relevant data, more data are needed to further verify the proposed method in the future.

3) In the large aperture angle SAR system, the 2-D spatial variation of motion error does affect the image quality. However, the proposed method focuses on the application of THz SAR, which has the characteristics of small imaging scenes. Based on the available data, we find that the azimuth spatial variation of the motion error is negligible, while the range spatial variation of the motion error needs to be considered due to the shorter THz wavelength. However, even if we ignore the range spatial variation error, our experimental results do not differ much from the theoretical values. This shows that the range spatial variation error in the experiment is small and has little effect on the image quality.

In addition, if the THz SAR imaging scene becomes larger or the motion error increases, the influence of range spatial variation error will be intensified, resulting in the proposed method's failure. Fortunately, we can improve the construction process of our coarse-compensation term. By selecting several points for error estimation, the motion error component of the platform is deduced. And the range spatial variation is compensated precisely by constructing the range spatial variation error compensation term. This is feasible both in theory and practice.

VI. Conclusion

This article proposes a two-step motion compensation method for polar format images of THz SAR, specifically designed to address the challenges of high-resolution imaging in THz polar format images. The proposed method innovatively adjusts the action nodes of coarse and fine two-step compensation, and combines residual RCM estimation and APE autofocus technology to provide a solution to the negative impacts of 2-D resampling in THz SAR PFA imaging. The effectiveness of the proposed method is validated through the simulation experiment and real data processing. This approach provides another way to enhance the performance of resampling-based imaging algorithms, such as PFA. While specifically tailored to the PFA, the principles and insights of this method have the potential to be applied to other imaging techniques based on rescaling. This method is expected to have broader applications and a significant influence in the field of high-resolution radar imaging.

References

[1] Y. Jungang, H. Xiaotao, J. Tian, J. Thompson, and Z. Zhimin, "New approach for SAR imaging of ground moving targets based on a keystone transform," *IEEE Geosci. Remote Sens. Lett.*, vol. 8, no. 4, pp. 829–833, Jul. 2011, doi: 10.1109/LGRS.2011.2118739.

[2] R. Zhu, J. Zhou, G. Jiang, and Q. Fu, "Range migration algorithm for near-field MIMO-SAR imaging," *IEEE Geosci. Remote Sens. Lett.*, vol. 14, no. 12, pp. 2280–2284, Dec. 2017, doi: 10.1109/LGRS.2017.2761838.

[3] J. Chen, D. An, W. Wang, Y. Luo, L. Chen, and Z. Zhou, "Extended polar format algorithm for large-scene high-resolution WAS-SAR imaging," *IEEE J. Sel. Topics Appl. Earth Observ. Remote Sens.*, vol. 14, pp. 5326–5338, May 2021, doi: 10.1109/JSTARS.2021.3081515.

[4] D. Liu, H. Shi, H. Liu, T. Yang, and J. Guo, "Enhanced forward-looking missile-borne bistatic SAR imaging with electromagnetic vortex," *IEEE Sensors J.*, vol. 23, no. 8, pp. 8478–8490, Apr. 2023, doi: 10.1109/JSEN.2022.3233084.

[5] L. Chen, R. Luo, J. Xing, Z. Li, Z. Yuan, and X. Cai, "Geospatial transformer is what you need for aircraft detection in SAR imagery," *IEEE Trans. Geosci. Remote Sens.*, vol. 60, 2022, Art. no. 5225715, doi: 10.1109/TGRS.2022.3162235.

[6] C. Wang, Q. Zhang, J. Hu, C. Li, S. Shi, and G. Fang, "An efficient algorithm based on CSA for THz stepped-frequency SAR imaging," *IEEE Geosci. Remote Sens. Lett.*, vol. 19, 2022, Art. no. 4006505, doi: 10.1109/LGRS.2020.3039958.

[7] G. Wang, F. Qi, Z. Liu, C. Liu, C. Xing, and W. Ning, "Comparison between back projection algorithm and range migration algorithm in terahertz imaging," *IEEE Access*, vol. 8, pp. 18772–18777, 2020, doi: 10.1109/ACCESS.2020.2968085.

[8] J. Ding, M. Kahl, O. Loffeld, and P. H. Bolívar, "THz 3-D image formation using SAR techniques: Simulation, processing and experimental results," *IEEE Trans. THz Sci. Technol.*, vol. 3, no. 5, pp. 606–616, Sep. 2013, doi: 10.1109/TTHZ.2013.2271298.

[9] S. Gui, J. Li, F. Zuo, and Y. Pi, "Analysis of security imaging method for walking human screening with single channel synthetic aperture radar," *IEEE Access*, vol. 7, pp. 111363–111374, 2019, doi: 10.1109/ACCESS.2019.2931413.

[10] F. Sheikh et al., "Towards continuous real-time plant and insect monitoring by miniaturized THz systems," *IEEE J. Microw.*, vol. 3, no. 3, pp. 913–937, Jul. 2023, doi: 10.1109/JMW.2023.3278237.

[11] S. Shi, C. Li, G. Fang, and X. Zhang, "A THz SAR autofocus algorithm based on minimum-entropy criterion," in *Proc. 44th Int. Conf. Infrared, Millimeter, THz Waves*, 2019, pp. 1–2, doi: 10.1109/IRMMW-THz.2019.8874225.

[12] Z. Hao, J. Sun, and D. Gu, "A novel motion compensation method for high resolution terahertz SAR imaging," in *Proc. 15th Int. Congr. Image Signal Process., Biomed. Eng. Inform.*, 2022, pp. 1–6, doi: 10.1109/CISP-BMEI56279.2022.9979931.

[13] G. Fornaro, "Trajectory deviations in airborne SAR: Analysis and compensation," *IEEE Trans. Aerosp. Electron. Syst.*, vol. 35, no. 3, pp. 997–1009, Jul. 1999, doi: 10.1109/7.784069.

[14] M. Xing, X. Jiang, R. Wu, F. Zhou, and Z. Bao, "Motion compensation for UAV SAR based on raw radar data," *IEEE Trans. Geosci. Remote Sens.*, vol. 47, no. 8, pp. 2870–2883, Aug. 2009, doi: 10.1109/TGRS.2009.2015657.

[15] G. Xu, Y.-L. Wang, and Y. Gong, "The novel method with sequence SAR imagery for INS/SAR integrated navigation system," in *Proc. 6th Asia-Pacific Conf. Synthetic Aperture Radar*, 2019, pp. 1–4, doi: 10.1109/APSAR46974.2019.9048511.

[16] J. Song and C. Xu, "A SAR motion compensation algorithm based on INS and GPS," in *Proc. IET Int. Radar Conf.*, 2020, pp. 576–581, doi: 10.1049/icp.2021.0815.

[17] H. Lin, X. Xue, N. Li, and M. Xing, "Two-dimensional autofocus combined with the TSA for spotlight SAR," *IEEE J. Sel. Topics Appl. Earth Observ. Remote Sens.*, vol. 16, pp. 9563–9573, 2023, doi: 10.1109/JSTARS.2023.3320555.

[18] M. Chen, X. Qiu, R. Li, W. Li, and K. Fu, "Analysis and compensation for systematical errors in airborne microwave photonic SAR imaging by 2-D autofocus," *IEEE J. Sel. Topics Appl. Earth Observ. Remote Sens.*, vol. 16, pp. 2221–2236, Feb. 2023, doi: 10.1109/JSTARS.2023.3245827.

[19] Z. Meng, L. Zhang, Y. Ma, G. Wang, and H. Jiang, "Accelerating minimum entropy autofocus with stochastic gradient for UAV SAR imagery," *IEEE Geosci. Remote Sens. Lett.*, vol. 19, 2022, Art. no. 4017805, doi: 10.1109/LGRS.2021.3106636.

[20] J. Chen, B. Liang, J. Zhang, D. Yang, Y. Deng, and M. Xing, "Efficiency and robustness improvement of airborne SAR motion compensation with high resolution and wide swath," *IEEE Geosci. Remote Sens. Lett.*, vol. 19, 2022, Art. no. 4004005, doi: 10.1109/LGRS.2020.3031304.

[21] A. W. Doerry, "Autofocus correction of excessive migration in synthetic aperture radar images," Sandia Nat. Lab., Albuquerque, NM, USA, Sandia Rep. SAND2004-4770, 2004, doi: 10.2172/919639.

[22] X. Zhong, H. Guo, M. Xiang, and H. Yue, "Residual motion estimation with point targets and its application to airborne repeat-pass SAR interferometry," *Int. J. Remote Sens.*, vol. 33, no. 3, pp. 762–780, Feb. 2012, doi: 10.1080/01431161.2011.577838.

[23] W. Xu, B. Wang, M. Xiang, C. Song, and Z. Wang, "A novel autofocus framework for UAV SAR imagery: Motion error extraction from symmetric triangular FMCW differential signal," *IEEE Trans. Geosci. Remote Sens.*, vol. 60, 2022, Art. no. 5218915, doi: 10.1109/TGRS.2021.3133331.

[24] D. W. Warner, D. C. Ghiglia, A. Fitzgerrell, and J. Beaver, "Two-dimensional phase gradient autofocus," in *Proc. Int. Symp. Opt. Sci. Technol.*, 2000, pp. 162–173.

[25] D. Zhu, "SAR signal-based motion compensation through combining PGA and 2-D map drift," in *Proc. 2nd Asian-Pacific Conf. Synthetic Aperture Radar*, 2009, pp. 435–438, doi: 10.1109/APSAR.2009.5374289.

[26] Y. Li, Q. Wu, J. Wu, P. Li, Q. Zheng, and L. Ding, "Estimation of high-frequency vibration parameters for terahertz SAR imaging based on FrFT with combination of QML and RANSAC," *IEEE Access*, vol. 9, pp. 5485–5496, 2021, doi: 10.1109/ACCESS.2020.3047856.

[27] S. Shi, C. Li, J. Hu, X. Zhang, and G. Fang, "A high frequency vibration compensation approach for terahertz SAR based on sinusoidal frequency modulation Fourier transform," *IEEE Sensors J.*, vol. 21, no. 9, pp. 10796–10803, May 2021, doi: 10.1109/JSEN.2021.3056519.

[28] J. Sun, Z. Hao, Q. Li, and D. Li, "Vibration compensation of airborne terahertz SAR based on along track interferometry," *IEEE Geosci. Remote Sens. Lett.*, vol. 19, 2022, Art. no. 4019105, doi: 10.1109/LGRS.2021.3116677.

[29] S. Shi, C. Li, J. Hu, X. Zhang, and G. Fang, "Motion compensation for terahertz synthetic aperture radar based on subaperture decomposition and minimum entropy theorem," *IEEE Sensors J.*, vol. 20, no. 24, pp. 14940–14949, Dec. 2020, doi: 10.1109/JSEN.2020.3010086.

[30] J. Chen, W. Wang, D. An, and Z. Zhou, "Airborne THz SAR imaging using RD algorithm integrated with autofocus," in *Proc. 6th Asia-Pacific Conf. Synthetic Aperture Radar*, 2019, pp. 1–5, doi: 10.1109/APSAR46974.2019.9048277.

[31] Y. Li et al., "A novel 2-D autofocusing algorithm for real airborne stripmap terahertz synthetic aperture radar imaging," *IEEE Geosci. Remote Sens. Lett.*, vol. 20, 2023, Art. no. 4012405, doi: 10.1109/LGRS.2023.3323266.

[32] J. Jiang, Y. Li, Y. Yuan, and Y. Zhu, "Generalized persistent polar format algorithm for fast imaging of airborne video SAR," *Remote Sens.*, vol. 15, no. 11, May 2023, Art. no. 2807, doi: 10.3390/rs15112807.

[33] B. D. Rigling and R. L. Moses, "Polar format algorithm for bistatic SAR," *IEEE Trans. Aerosp. Electron. Syst.*, vol. 40, no. 4, pp. 1147–1159, Oct. 2004, doi: 10.1109/TAES.2004.1386870.

[34] X. Mao and D. Zhu, "Two-dimensional autofocus for spotlight SAR polar format imagery," *IEEE Trans. Comput. Imag.*, vol. 2, no. 4, pp. 524–539, Dec. 2016, doi: 10.1109/TCI.2016.2612945.

[35] T. Shi, X. Mao, A. Jakobsson, and Y. Liu, "Extended PGA for spotlight SAR-filtered backprojection imagery," *IEEE Geosci. Remote Sens. Lett.*, vol. 19, 2022, Art. no. 4516005, doi: 10.1109/LGRS.2022.3223164.
[36] J. Cai, M. Martorella, S. Chang, Q. Liu, Z. Ding, and T. Long, "Efficient nonparametric ISAR autofocus algorithm based on contrast maximization and Newton's method," *IEEE Sensors J.*, vol. 21, no. 4, pp. 4474–4487, Feb. 2021, doi: 10.1109/JSEN.2020.3029830.
[37] Z. Ding et al., "An autofocus back projection algorithm for GEO SAR based on minimum entropy," *IEEE Trans. Geosci. Remote Sens.*, vol. 60, 2022, Art. no. 5226114, doi: 10.1109/TGRS.2022.3164922.
[38] W. Pu, J. Yang, W. Li, J. Wu, and Y. Lv, "A residual range cell migration correction algorithm for SAR based on low-frequency fitting," in *Proc. IEEE Radar Conf.*, 2015, pp. 1300–1304, doi: 10.1109/RADAR.2015.7131196.

Shaowen Luo received the B.E. degree in optoelectronic information science and engineering from the Jiangxi University of Science and Technology, Ganzhou, China, in 2020, and the M.E. degree in electronic information from the University of Shanghai for Science and Technology, Shanghai, China, in 2024.

His main research interests include signal processing for terahertz radar systems, including imaging algorithms and motion error compensation algorithms.

Qiuyan Wang received the B.E. degree in electronic information engineering degree from Nanchang Hangkong University, Nanchang, China, in 2022. She is currently working toward the M.S. degree in electronic information engineering with the Shanghai University of Science and Technology, Shanghai, China.

Her main research interests include ISAR imaging and recognition.

Yinwei Li (Member, IEEE) received the B.E. degree in electronic information engineering from the University of Electronic Science and Technology of China, Chengdu, China, in 2009, and the Ph.D. degree in signal and information processing from the University of Chinese Academy of Sciences, Beijing, China, in 2014.

He was with Shanghai Radio Equipment Research Institute, Shanghai, China, from 2014 to 2019. He is with Terahertz Technology Innovation Research Institute, Terahertz Spectrum and Imaging Technology Cooperative Innovation Center, University of Shanghai for Science and Technology, Shanghai, China. He is also with the School of Intelligent Emergency Management, University of Shanghai for Science and Technology, and the Shanghai Institute of Intelligent Science and Technology, Tongji University, Shanghai, China. He is currently an Associate Professor with the University of Shanghai for Science and Technology. His research interests include (inverse) synthetic aperture radar (SAR) imaging, interferometric SAR system design and signal processing, terahertz radar imaging, and so on.

Xiaolong Chen received the B.E. degree in optoelectronic information science and engineering from Anqing Normal University, Anqing, China, in 2023. He is currently working toward the M.E. degree in optical engineering with the University of Shanghai for Science and Technology, Shanghai, China.

The main research contents include noncontact heart rate respiration detection based on millimeter wave radar.

Yiming Zhu (Senior Member, IEEE) received the Ph.D. degree in electronic engineering from the University of Tokyo, Tokyo, Japan, in 2008.

He is currently with the Shanghai Key Lab of Modern Optical System and the Terahertz Technology Innovation Research Institute, University of Shanghai for Science and Technology, Shanghai, China, and also with Terahertz Spectrum and Imaging Technology Cooperative Innovation Center, Shanghai, China. He is the Director of Terahertz Spectrum and Imaging Technology Cooperative Innovation Center and Terahertz Precision Biomedical Technology Overseas Expertise Introduction Center for Discipline Innovation, University of Shanghai for Science and Technology. Up to now, he has authored or coauthored more than 100 articles, including more than 40 articles in the *Light: Science and Applications*, *Advanced Optical Materials*, *Applied Physics Letters*, *Optics Letters*, and *Optics Express* (Top 5%), including five articles are selected as ESI articles. His research interests include terahertz technologies and applications, including terahertz devices, terahertz spectroscopy, imaging systems, terahertz bioapplications, and so on. He is currently an Award Committee Member of the International Society of Infrared, Millimeter Wave and Terahertz and a Council Member of China Instrument and Control Society, China Optical Engineering Society, and the Young Scientist Club of China Electronics Society. He is also the Topic Editor for "*Light: Advanced Manufacturing*," "*PhotoniX,*" and so on.